Appl. Phys. B 77, 469–484 (2003)
DOI: 10.1007/s00340-003-1260-1

Applied Physics B
Lasers and Optics

Invited paper

U. WOGGON[1,✉]
R. WANNEMACHER[2]
M.V. ARTEMYEV[3]
B. MÖLLER[1]
N. LETHOMAS[1]
V. ANIKEYEV[1]
O. SCHÖPS[1]

Dot-in-a-dot: electronic and photonic confinement in all three dimensions

[1] Fachbereich Physik, Universität Dortmund, Otto-Hahn Str. 4, 44221 Dortmund, Germany
[2] Fakultät für Physik und Geowissenschaften, Universität Leipzig, Linnéstr. 5, 04103 Leipzig, Germany
[3] Institute for Physico-Chemical Problems of Belarussian State University, Leningradskaya str., 14, Minsk 220080, Belarus

Received: 26 June 2003
Published online: 23 September 2003 •

ABSTRACT We have studied the optical properties of three-dimensionally confined photon states in a spherical microcavity (the photonic dots) resonantly excited by photons emitted from semiconductor nanocrystals (the quantum dots). Glass and polymer microspheres with sizes of $2\lambda < R < 10\lambda$ are characterized by spatially and temporally resolved micro-photoluminescence. The role of nanocrystal position and orientation is analyzed experimentally and theoretically. The emission spectra of single, bulk and hollow microspheres impregnated with CdSe quantum dots and quantum rods are investigated and the modification of the quantum dot radiative lifetime by the three-dimensional photon confinement is discussed.

PACS 78.66.Hf; 61.46.+w; 42.60.Da

1 Introduction

Optical microcavities, which confine the propagation of light in all three dimensions are fascinating research objects to study light–matter interactions in low-dimensional systems. They are often called photonic dots (PD) [1, 2], in analogy to the three-dimensional (3D) electronic confinement in semiconductor quantum dots (QDs). The basic concepts of light–matter interaction in semiconductor microcavities have been demonstrated already in the 1990s (see for example [3–6] and Refs. therein). Currently, there is an emerging interest in coupling 3D-confined electronic states (QDs) with 3D-confined photon states, and promising applications in advanced optical technologies, quantum optics, and microsensing are discussed in [7, 8]. In the last few years a tremendous increase has been observed in reports about high-finesse spherical microcavities and exploring their use for frequency standards, modulators, narrow-band light emitters and detectors, ultralow-threshold lasers, building blocks for photonic structures, or templates for molecule transport and biosensors (see for example [9–13]).

A substantial part of the research is aimed at the demonstration of the basic principles of cavity-quantum electrodynamics (cavity-QED) by making use of spherical microcavities. Applications were proposed for threshold-less lasers, single-photon emitters, and quantum information processing. A complex optimization problem has to be solved in order to obtain the optimum microcavity with a small mode volume, a high cavity finesse and efficient in- and out-coupling of emission [14]. The active emitters themselves became the subject of research, especially their positioning, addressing and control. The usual atoms are replaced by artificial semiconductor nanostructures, such as self-organized QDs or nanocrystals, with new types of energy levels, fine structure and optical transition dipole moments etc.

The studies presented in the following are aimed at the understanding of exciton–electromagnetic field interaction of II–VI compound semiconductor quantum dots in spherical microcavities. We study CdSe quantum dots and quantum rods which show very efficient emission in the visible spectral range. The investigated microspheres have radii R comparable to the wavelength λ of the quantum dot emission, i.e. between $2\lambda < R < 10\lambda$. The discrete photon states of a spherical cavity are characterized by angular (ℓ), azimuthal (m) and radial (n) quantum numbers for the transverse electric ($\mathrm{TE}^n_{\ell,m}$) and transverse magnetic ($\mathrm{TM}^n_{\ell,m}$) field modes. The microcavities studied typically had a large free spectral range of up to 30 nm, much larger than the homogeneous line-broadening of single-dot emission, which opens the way towards single-mode–single-dot coupling.

To describe the "atom"–field interaction (i.e. here the 3D-confined exciton in the photonic dot), we need to know the radiative decay rate of quantum dot excitons without cavity Γ_{rad}, the decay rate of photons in the cavity Γ_{cav}, and the Rabi frequency $\Omega = \boldsymbol{\mu}\boldsymbol{E}/\hbar$ with $\boldsymbol{\mu}$ the quantum dot optical transition dipole moment and $\boldsymbol{E}$ the electric field. Ω is a measure describing the matter–field coupling strength. In the weak coupling regime, for example, the relation $\Omega \ll \Gamma_{\mathrm{rad}}, \Gamma_{\mathrm{cav}}$ holds, i.e. spontaneous emission is still dominant. The spontaneous radiative decay of the exciton is irreversible, whereas in the strong coupling regime spontaneous emission becomes a reversible process with $\Omega \gg \Gamma_{\mathrm{rad}}, \Gamma_{\mathrm{cav}}$. The quantum dot exciton and the cavity then exchange energy coherently.

To evidence the existence of either weak or strong coupling one is in search of such experimental signatures as the enhancement of the spontaneous emission rates of confined excitons in a cavity described by the Purcell factor

$$F = \frac{3Q}{4\pi^2 V}\left(\frac{\lambda_{\mathrm{cav}}}{n}\right)^3 \qquad (1)$$

✉ Fax: +49-231/755-3674,
E-mail: woggon@fred.physik.uni-dortmund.de

in the case of weak coupling [15] or cavity mode splittings by the Rabi splitting energy

$$\hbar\Omega = |\boldsymbol{\mu}\boldsymbol{E}| = \hbar\frac{\lambda}{2\pi}\sqrt{\frac{3\pi c}{2n^3\tau_{\mathrm{rad}}V}} \tag{2}$$

in the case of strong coupling [16, 17]. As can be seen from (1) and (2), the important parameters here are: (i) the mode volume V of the microcavity as a measure of the electromagnetic field strength $\boldsymbol{E}$; (ii) the optical transition dipole moment $\boldsymbol{\mu}$ of the nanoemitter, which gives us directly τ_{rad} and the radiative limit in homogeneous line broadening $\hbar\Gamma_{\mathrm{rad}}$ [91]; and (iii) the cavity quality factor $Q = \omega/\Gamma_{\mathrm{cav}}$, defined as the ratio between the resonance energy and the cavity mode width. Q contains the information about the lifetime of photons in resonance with a cavity mode. n is the refractive index of the semiconductor material and c the vacuum velocity of light.

In this work we give an overview of the current understanding of light–matter interaction in a microsphere–nanocrystal system. We use it as a simple model system to test the potential of microspheres as a tool for demonstrating cavity QED effects. We show that the use of semiconductor nanocrystals as photon emitters in 3D-microcavities requires a careful investigation of the position, orientation and internal fine structure of the light-emitting materials, as well as cavity size, shape, refractive index contrast, etc. in order to selectively excite cavity modes with high-Q values and smallest mode volume V. We start with Sect. 2, in which we characterize the microcavity properties, modelling the nanoemitters as dipoles and focussing on the effects of a variation of the nanoemitter position and orientation. In Sect. 3 we introduce the CdSe quantum dots and rods and give data about their radiative decay times τ_{rad}. Sect. 4 finally summarizes the results obtained when quantum dots/rods are incorporated in photonic dots.

2 Dipole excitation in a spherical microcavity

Since the work of Mie [18] and Debye [19], the solution to the problem of scattering of electromagnetic waves by a dielectric sphere is well known. Conventional Mie theory assumes that the incident electromagnetic field is a linearly or circularly polarized plane wave which can be represented by an infinite sum of multipoles. The basic theory is reviewed in a number of standard references (see for example [20–25] and Refs. therein). Detailed work is presently being performed to study non-linear optical properties, lasing and cavity QED properties of microspheres containing nanometer-sized light-emitting entities (see for example [26–35] and Refs. therein). The special aspect we want to address in this section is the coupling of nanoscopic emitters to the optical modes of microspheres as a function of position and orientation of an active optical dipole, the semiconductor nanocrystal, in the spherical cavity. Our aim is to provide an overview of peculiarities in the case of dipole excitation of a spherical microcavity.

Basic studies of the properties of light emitters coupled to microcavities started first with dye-doped microdroplets and soon also covered glass microspheres. The first proposals to engineer both position and orientation of light emitters can be found in [36–39] using microdroplets doped with special dye molecules. The use of semiconductor QDs as photon emitters in 3D-microcavities requires a careful consideration of the coupling of anisotropic emission to the optical modes of the microsphere cavity. Most QDs are known to have anisotropies in their shape, crystal structure or confining potentials. The control of both position and orientation of the light-emitting species is thus highly relevant, for example, for controlling the selective excitation of either TE or TM modes, or for achieving high coupling efficiency of spontaneous emission into cavity modes.

2.1 *Dipole position*

With Fig. 1 and Fig. 2, we illustrate the effect of quantum dot position on the coupling of the quantum dot

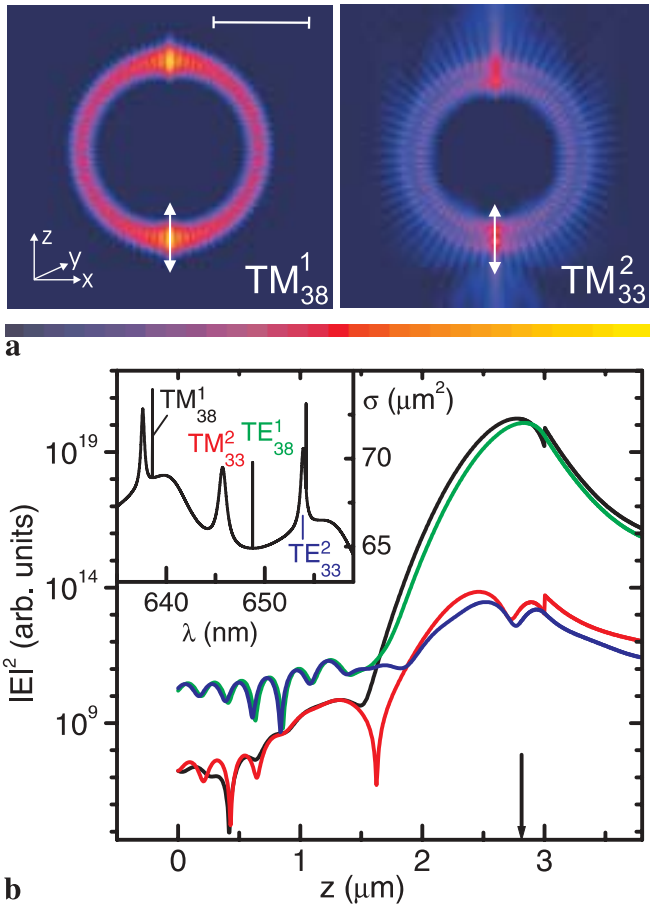

FIGURE 1 **a** Calculated electromagnetic field intensity ($|E|^2$) in and outside a spherical microcavity of $R = 3\,\mu$m radius for the case of excitation by a single dipole at $z = -2.8\,\mu$m. The *arrows* indicate the dipole orientation $\boldsymbol{d} \parallel z$. *Left*: dipole resonant with the $\mathrm{TM}^1_{38,0}$ mode ($\lambda = 638.595$ nm, the color-coded intensity scale is logarithmic and covers 40 dB), *right*: dipole resonant with the $\mathrm{TM}^2_{33,0}$ mode ($\lambda = 645.717$ nm, the color-coded intensity covers 60 dB). The marker corresponds to 3 μm. **b** Square of the magnitude of the electric field as a function of radial coordinate z for positive z values, opposite to the location of the dipole, calculated for the case of resonance with one of the four modes $\mathrm{TM}^1_{38,0}$, $\mathrm{TE}^1_{38,1}$, $\mathrm{TM}^2_{33,0}$, and $\mathrm{TE}^2_{33,1}$ and plotted on a logarithmic scale. The *arrow* indicates the position of the dipole on the opposite side of the sphere ($z = -2.8\,\mu$m). For TM modes $\boldsymbol{d} \parallel z$ and for TE modes $\boldsymbol{d} \parallel x$ is assumed. Note that for TM-resonances there is a discontinuity at the microsphere surface due to the radial component of the electric field present in these modes. *Insert*: Mie spectrum for a sphere with $R = 3\,\mu$m and refractive index $n = 1.5$

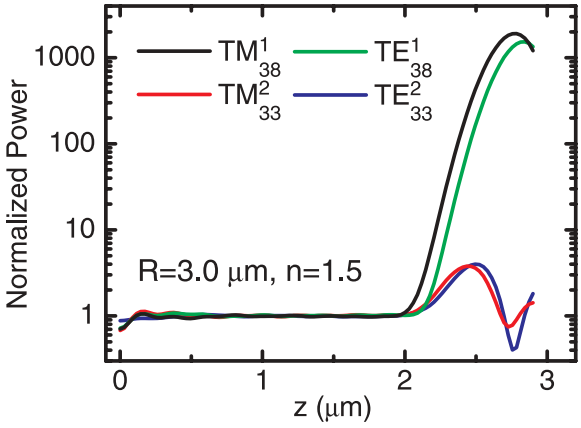

FIGURE 2 The calculated total power emitted by an oscillating dipole as a function of dipole position, normalized to the power emitted by the same dipole in bulk glass. Note the logarithmic scale. The dipole is oriented radially ($||z$, see Fig. 1) in the case of TM resonances and tangentially to the sphere surface ($||x$) in the case of TE modes. The corresponding wavelengths of the different modes are 638.595 nm (TM^1_{38}), 645.717 nm (TM^2_{33}), 648.769 nm (TE^1_{38}), 653.905 nm (TE^2_{33}).

emission to modes of the microsphere with radial quantum numbers $n = 1$ and $n = 2$. The electromagnetic field distribution in and outside the spherical microcavity is calculated semi-analytically using the multiple multipole (MMP) technique [40] for the case of resonance with exemplary TM and TE modes of a microsphere ($R = 3\,\mu$m radius, refractive index $n = 1.5$), excited by a resonant dipole positioned 0.2 μm below the sphere surface. Fig. 1a shows the result for the case of resonance with two TM modes with different radial quantum numbers at adjacent wavelengths: TM^1_{38} at 638.595 nm and TM^2_{33} at 645.717 nm. In both cases the field is highly concentrated at the poles of the sphere and close to the sphere surface. The angular quantum number ℓ indicates how many maxima can be observed in the internal field distribution as a function of the polar angle from 0 to 180°, while the radial quantum number n gives the number of maxima (or, alternatively, the number of nodes) of the intensity in the radial coordinate. As can be seen, for higher radial quantum numbers the $\boldsymbol{E}$-field starts to extend into the inner part of the sphere, resulting in an increase of the effective mode volume.

In Fig. 1b the radial intensity distribution is shown for dipole excitation in resonance with the TM modes of Fig. 1a, as well as for resonance with TE modes in the same range of wavelengths. For the $n = 1$ modes, the field is maximum at $z = 0.95\ R$ in the case of the TE^1_{38} mode and at $z = 0.93\ R$ for the TM^1_{38} mode. The $n = 2$ modes exhibit two main intensity maxima inside the sphere as a function of the radial coordinate. Here the field is maximum at $z = 0.84\ R$ in the case of the TE^2_{33} mode and at $z = 0.82\ R$ for the TM^2_{33} mode. The effect of strong field concentration close to the sphere surface in the case of $n = 1$ modes becomes even more pronounced for microspheres with sizes considerably larger than the wavelength λ. For smaller spheres with $R < \lambda$, the field distribution develops more towards a homogeneous one [41].

It should be remarked that even though the dipole is resonant with the indicated mode in each case, a large number of other modes are also excited by the same dipole and contribute to the field. This also explains why the intensity minimum for the $n = 2$ modes between the two main maxima in Fig. 1b does not correspond to zero intensity, in contrast to the pure $n = 2$ modes of the bare sphere. Furthermore, we will show cases below where the dipole, although resonant with an optical mode of the sphere, is not able to excite the resonance at all.

In Fig. 2 the total emitted power is plotted as a function of dipole position along the z axis. It shows that the optimum dipole position is just below the sphere surface ($z = 0.93\ R$ for the TM^1_{38} mode, $z = 0.95\ R$ for the TE^1_{38} mode, $z = 0.83\ R$ for the TE^2_{33} mode, and $z = 0.81\ R$ for the TM^2_{33} mode), and coincides rather precisely with the intensity maxima of the corresponding modes. Moreover, the total emitted power maps out qualitatively the intensity distribution of the resonant modes in the spatial region where these modes have appreciable intensity. The emitted power is reduced, however, close to the center of the sphere for all modes considered. In addition, for resonances with the $n = 2$ modes, a suppression of the emitted power occurs in the region between the two intensity maxima of these modes. The reduction of the emitted power amounts to 60% in the intensity minimum of the TE^2_{33} mode, compared to a dipole embedded in bulk glass. This corresponds to a lengthening of the radiative lifetime in the weak-coupling limit. In contrast, a dipole located at the optimum position obviously couples very efficiently to the high-Q modes with $n = 1$, as can be seen from the very large values of the normalized emitted power (1910 for the TM^1_{38} mode). For a dipole located in the interior of the sphere, the total emitted power approaches that of a dipole embedded in bulk glass, except at the center of the dipole.

To optimize the emitter position, we proposed in [42] the concept of a hollow polymeric microsphere doped with CdSe nanocrystals and demonstrated the efficient excitation of distinct, spectrally well-separated $n = 1$ cavity modes while cavity modes of higher radial quantum numbers $n > 1$ were suppressed (see Sect. 4.1).

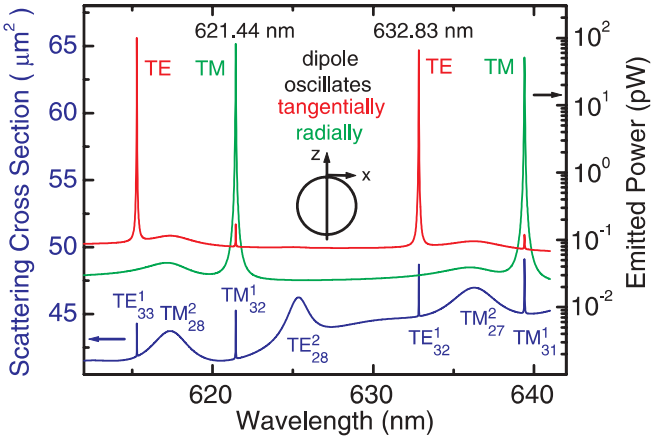

FIGURE 3 Scattering spectrum of a microsphere ($R = 2.5\,\mu$m radius, $n = 1.5$) in vacuum, excited by a plane wave, calculated via standard Mie theory (blue graph, linear scale on the left) and power emitted by the sphere, when the latter contains a radiating dipole (1 Debye) 0.2 μm below the sphere surface and oriented parallel to the z axis (*green graph*) or parallel to the x axis (*red graph*), respectively (logarithmic scale on the *right*). The emission spectra for dipole excitation are calculated by means of the MMP technique

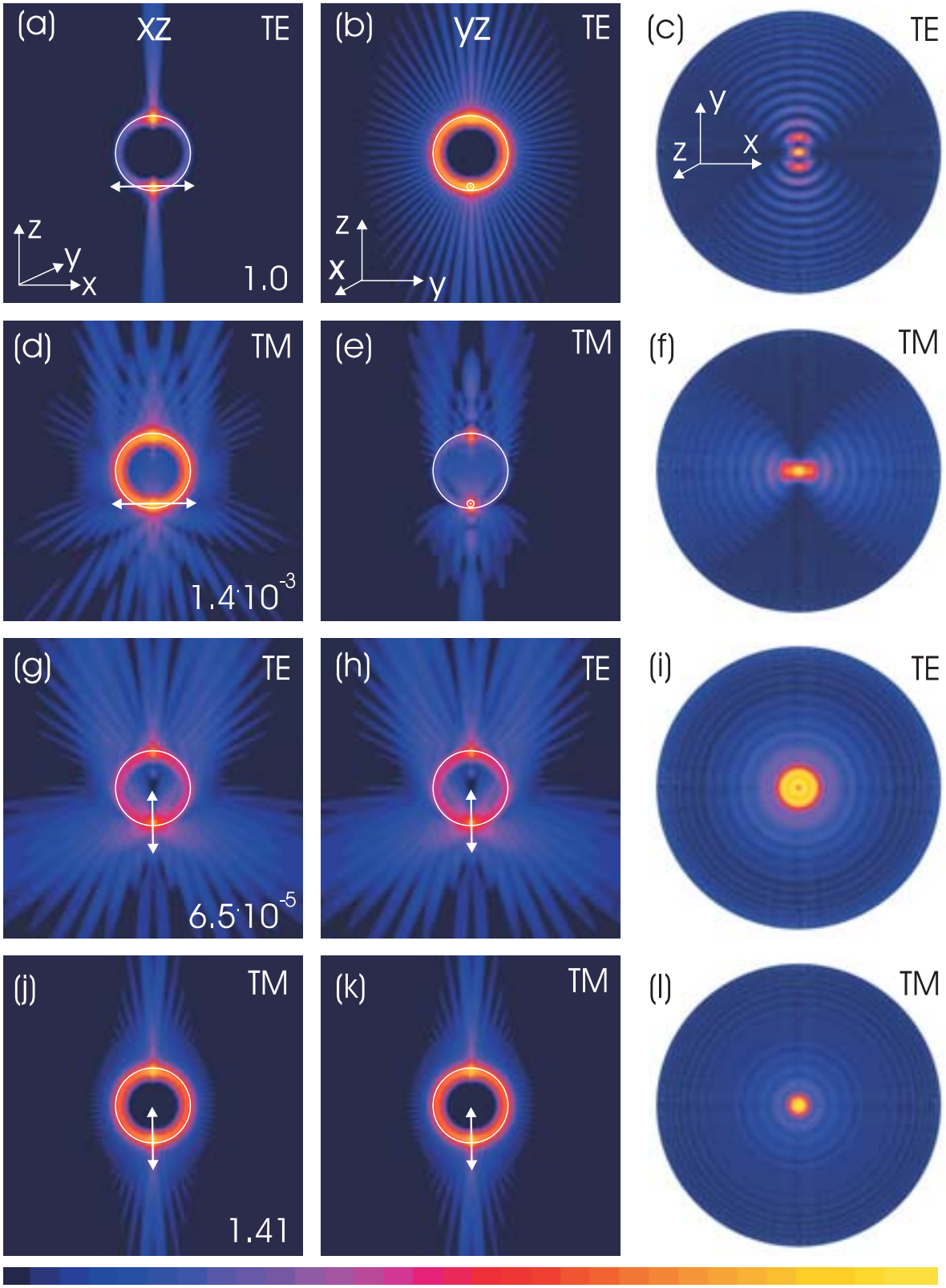

FIGURE 4 Calculated electromagnetic intensity ($|E|^2$) in and outside a spherical microcavity (sphere radius $R = 2.5\,\mu$m, refractive index $n = 1.5$) for the case of excitation by a single dipole located on the z-axis at $z = -2.3\,\mu$m aligned in two different directions. The dipole emission is chosen to be resonant to the TE^1_{32}-mode ($\lambda = 632.83$ nm, figures (**a**–**c**) and (**g**–**i**)), or to the TM^1_{32}-mode ($\lambda = 621.44$ nm, figures (**d**–**f**) and (**j**–**l**)), respectively. The two columns on the left contain plots of the intensity in the xz- (**a**,**d**,**g**,**j**) and yz-planes (**b**,**e**,**h**,**k**) for the dipole oscillating in the x- (**a**–**f**) and z-directions (**g**–**l**), respectively. Each rectangular plot represents an area of $20 \times 20\,\mu$m^2. The intensity scale is logarithmic in the two columns of images on the left and covers 60 dB. The maximum intensity in **a**–**c** is normalized to 1.0. In (**d**,**g**,**j**) the maximum field intensity is given with respect to (**a**).The third column shows the three-dimensional intensity distributions on the inner surface of the sphere on a *linear* intensity scale. Note that the mode designations TE and TM only indicate the mode in resonance with the dipole. In **d**–**i** these modes are not actually excited, and, hence, the field distribution is not even approximately that of the resonant mode (see text)

2.2 *Dipole orientation*

In Figs. 3 and 4 we analyze the role of the orientation of the light-emitting dipole, represented, for example, by an anisotropic CdSe nanocrystal as the nanoscopic light emitter. Figure 3 shows an illustrative calculation of the total power emitted by a single oscillating dipole, $d = 1$ Debye, in a spherical cavity ($R = 2.5$ μm radius, refractive index $n = 1.5$) as a function of the wavelength and the dipole orientation, when the dipole is located close to the inner surface of the sphere. Comparison with the Mie scattering spectrum under plane-wave excitation (blue spectrum) shows that dipole excitation results in a weighting of the different TE and TM mode amplitudes. If the dipole, assumed to be located on the z-axis, oscillates in the z-direction, TM modes are exclusively excited (green spectrum). This is caused by the fact that only the TM modes have an electric field component in the radial direction. The dipole oscillation in the x-direction (tangential to the surface of the sphere), however, excites predominantly TE modes (red spectrum). In both cases $n = 1$ modes are strongly favored by dipole excitation for the assumed dipole position, and the excitation of these modes is extremely efficient compared to plane-wave excitation. For the resonances shown in Fig. 3, a maximum quality factor $Q = \omega_{\mathrm{cav}}/\Delta\omega_{\mathrm{cav}} = 10^5$ is calculated for the microsphere of $R = 2.5$ μm and refractive index $n = 1.5$ [43].

For the case of resonance with two representative TE and TM modes, the electromagnetic field intensity (modulus of the squared electric field amplitude) in and outside of the spherical microcavity is plotted in Fig. 4 for the two dipole orientations, radial ($\| z$) and tangential ($\| x$), respectively. In Fig. 4a–f, the dipole oscillates in the x-direction, in Fig. 4g–l in the z-direction. In agreement with the previous Fig. 3, it is easily recognized again that a dipole on the z axis at the assumed position and oscillating in the x direction excites predominantly TE modes, whereas the same dipole excites exclusively TM modes when it is oscillating in the z direction. The resonances are actually not or only weakly excited in the cases of figures (d–i). This result is different from the case of plane-wave excitation, but similar to the case of excitation by s- or p-polarized evanescent waves [44]. Moreover, from figures a–c and j–l, it is obvious that a dipole oscillating in the x direction excites TE modes with azimuthal quantum number $m = 1$, whereas a dipole oscillating in the z direction excites TM modes with $m = 0$. This fact is easily explained by the translation addition theorem of vector multipoles, which implies that the azimuthal quantum number is conserved when a given multipole is expanded into multipoles centered at a different position on the z axis. It should be noted that the $m = 1$ and $m = 0$ modes, which are strongly dominating in figures a–c and j–l, respectively, are very different from the whispering-gallery modes excited, for example, by evanescent waves.

The active control of the polarization state of microcavity photons has been demonstrated by us by using quantum-confined semiconductor nanorods as highly polarized nanoemitters. The efficient confinement of photons spontaneously emitted by nanorods into single transverse electric (TE) cavity modes is achieved, while transverse magnetic (TM) modes are suppressed. These experimental results will be discussed in Sect. 4.3.

3 CdSe nanocrystals as the dipole emitter

Semiconductor nanocrystals are attractive nanometer-sized photon emitters for applications in optical microcavities. Their wide spectral tunability, high quantum efficiency and possible manipulation on a single-dot basis make them good candidates as active optical materials. Quantum dots were found to possess a narrow emission spectrum and superior photostability, as compared to conventional dye molecules. Our nanocrystal-emitters have to be characterized with respect to such important properties as radiative lifetimes, homogeneous line broadening and polarization anisotropies in the emission characteristics. The ideal emitter should have a large optical transition dipole moment and emit light whose polarization couples efficiently to the modes of the microcavity. It should show a monoexponential luminescence decay determined only by its radiative lifetime without complicating fine structure. Its homogeneous spectral line width should be of the order of the highest Q cavity-mode widths in the QD spectral emission range. Such an emitter, however, is hard to find, and one is confronted with an optimization problem, which we will discuss in this Section.

3.1 *Synthesis*

The common method of synthesizing highly luminescent II–VI semiconductor nanocrystals is based on high-temperature reactions of organometallic precursors in a highly coordinating medium. For the synthesis of CdSe nanocrystals, usually trioctylphosphine selenide and dimethylcadmium are used as the precursors. The reaction is carried out in trioctylphosphine oxide (TOPO)/hexadecylamine mixture at a temperature above 200 °C (see, for example, [45, 46] and references therein).

The high processing temperature and optimized concentrations of reagents allow nanocrystals to be obtained with a photoluminescence (PL) quantum yield exceeding 70% at room temperature (see, for example, [47] and Refs. therein). Figure 5 (left part) shows representative absorption and photoluminescence spectra of two CdSe quantum dot ensembles prepared for our experiments. Controlled variation in the quantum dot size results in a spectral tunability of the emission wavelengths between 530 nm and 680 nm. Caused by the manifest size distributions, both absorption and PL spectra of nanocrystal ensembles are inhomogeneously broadened with a full-width at half-maximum (FWHM) of $\sim$ 80–120 meV.

The photoluminescence yield of CdSe nanocrystals is sensitive to the surrounding media and easily quenched by water, oxygen etc. In order to increase the stability of CdSe nanocrystals, they are chemically covered with layers of wide gap semiconductor material like ZnS, ZnSe, CdS. The core/shell CdSe/ZnS nanocrystals show excellent stability of photoluminescence even in biological environments [48, 49]. Non-optimum growth conditions and environments affect not only the PL efficiency but also modify the population dynamics (see for example [50, 51] and Refs. therein). To avoid non-radiative recombination via surface traps, only those nanocrystal preparation routes which result in both high

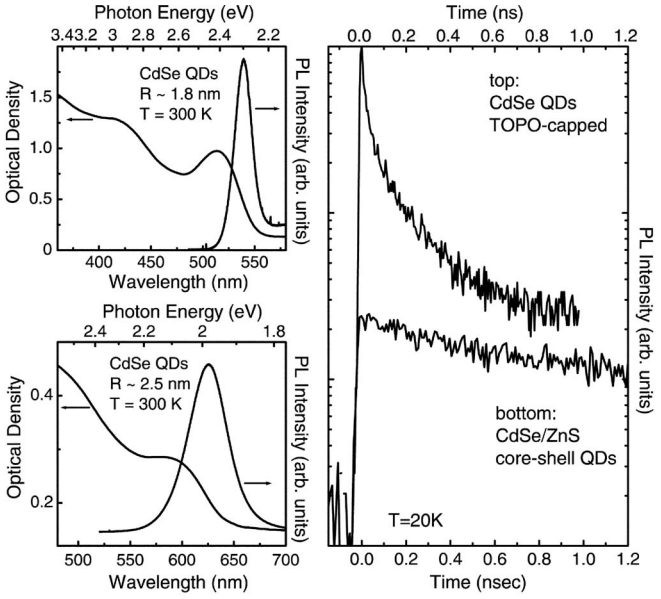

FIGURE 5 *Left*: Absorption and emission spectra of CdSe nanocrystals of different average sizes. As the result of size variations, the emission wavelengths can be tuned between 530 nm and 680 nm. The peaks in the absorption spectra indicate the quantum confined electron–hole pair states. *Right*: Photoluminescence decay of standard TOPO-capped CdSe quantum dots (*top*), and core-shell CdSe/ZnS quantum dots (*bottom*) measured at $T = 20$ K. The detection energy is tuned into the low-energy side of the emission spectrum

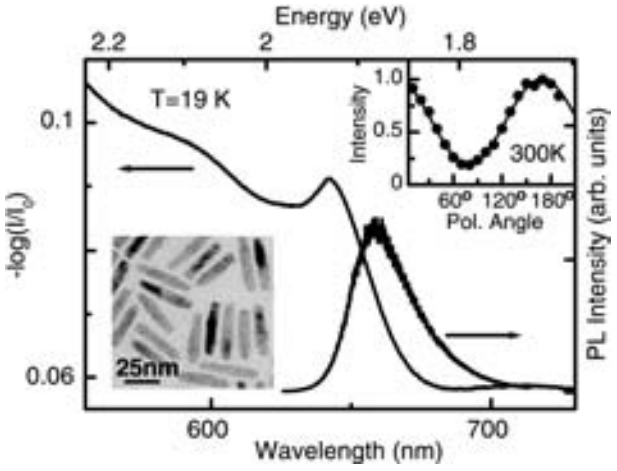

FIGURE 6 Low-temperature absorption and photoluminescence spectrum of CdSe nanorods. The average rod size derived from high-resolution TEM images is 7 nm in diameter and 35 nm in length. The *inset* shows the degree of linear polarization for single CdSe nanorod emission measured at $T = 300$ K

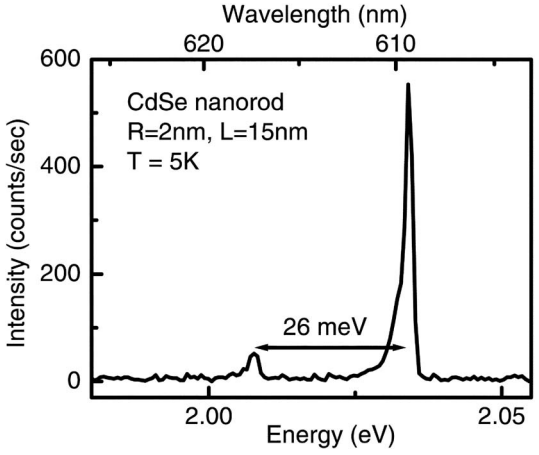

FIGURE 7 Low-temperature spectrum of a single CdSe nanorod measured at $T = 5$ K with an integration time of 1 s

quantum efficiency and no fast initial decay components in the luminescence dynamics are appropriate for our studies (see also Sect. 3.2). As can be seen from Fig. 5 (right part) core/shell CdSe/ZnS nanocrystals fulfil these conditions at low excitation power. In contrast to CdSe quantum dots with the usual TOPO-capping, no fast initial decay is observed, indicating the low concentration of surface traps. It should be mentioned here that fast initial decays can be enhanced or even produced by strong optical pumping (sometimes believed to represent the possibility of increasing the signal for nanocrystals of low efficiency). The creation of more than one electron–hole pair per nanocrystal opens additional recombination channels involving many-particle processes like biexciton decay or Auger recombination. In our experiments, we avoided the effects of high excitation density by measuring first the power-dependent decay times to derive the low-density limit experimentally.

Not only the size of nanocrystals can be controlled during the synthesis, but also the shape. Introducing special chemical regulators of growth into the reaction mixture, such as alkylphosphonic acids, one can obtain CdSe rods or even more exotic tetrapods and teardrops. As has been reported in [52–55], CdSe quantum rods can be synthesized with aspect ratios as large as 5 to 1 and with highly polarized emission.

For our studies, we prepared CdSe nanorods with optical properties shown in Fig. 6. The low-temperature absorption spectrum is characterized by a blue-shifted absorption peak due to quantum confinement and an efficient PL peak with an inhomogeneous broadening of 75 meV (excitation at 488 nm with 8 mW focussed to a spot of 70 μm). The inset evidences the high degree of linear polarization of about 70%, measured here for single nanorod emission at room temperature. The low-temperature single nanorod spectrum is shown in Fig. 7. The spectral line shape and width here are determined by the spectral jitter during the signal accumulation. The second peak in the single-rod emission spectrum is separated by the LO-phonon energy of CdSe and explained by a phonon-assisted process. Taking into account the long integration time, the measured PL linewidth of 1.5 meV is an upper limit for the single-rod homogeneous linewidth and even smaller values, similar to CdSe nanocrystals, can be expected.

3.2 *Dynamics of luminescence*

To study the modification of the quantum dot spontaneous-emission rate in a microcavity (Purcell effect, see Sect. 4.2), first we need to know the QD radiative decay time Γ_{rad} in free space. In the strong confinement regime, i.e. for QD sizes smaller than the bulk exciton Bohr radius, $R < a_{\mathrm{B}}$, optical transition probabilities are determined by the strength of the electron–hole exchange interaction causing a fine structure splitting of the transition to the electron–hole pair ground state $|0\rangle$. In Fig. 8, we give an overview of

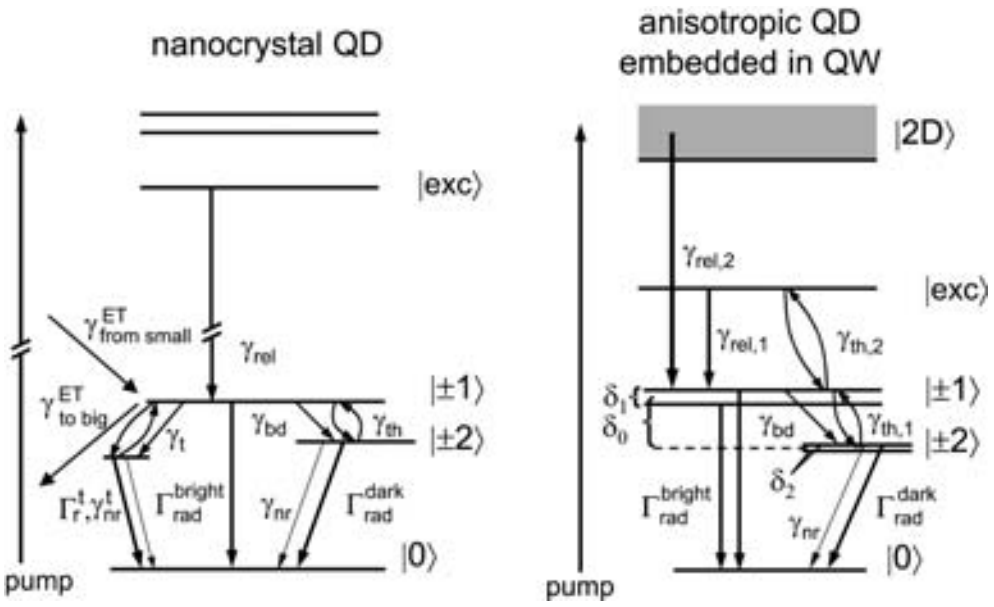

FIGURE 8 The scheme of the relaxation and recombination pathways of photo-excited electron–hole pairs in different types of CdSe quantum dots: colloidal nanocrystals (*left*) and epitaxially grown CdSe islands embedded in a ZnSe quantum well (*right*). $\Gamma_{\mathrm{rad}}^{\mathrm{bright}}$ is the radiative recombination rate for the optically allowed transition from $|\pm 1\rangle$ states to the ground state $|0\rangle$ and $\Gamma_{\mathrm{rad}}^{\mathrm{dark}}$ is the same for forbidden transitions from $|\pm 2\rangle$ states. γ_{bd} is the bright-dark state transition rate, γ_{nr} are non-radiative recombination rates, γ_{rel} are relaxation rates, γ_{th} are thermal population rates. The kinetic models for ensembles of colloidal nanocrystals additionally take into account energy transfer rates γ^{ET} between nanocrystals. γ_{t} characterizes a decay channel which can be thermally activated and then refills the bright state (see text). $|\mathrm{exc}\rangle$ denotes higher excited QD-states. In epitaxially grown QDs $|2\mathrm{D}\rangle$ denotes states in the surrounding quantum well. For δ_0, δ_1, and δ_2 see text

similarities and differences in the currently known recombination and relaxation processes for different types of QD samples. Colloidal CdSe nanocrystals and epitaxially grown CdSe islands embedded in ZnSe are promising candidates for microsphere and microdisc cavities and hence both compared here with respect to their similarities and differences. All QD types have the following in common: (i) the exchange interaction splits the lowest electron–hole pair state into dark states (total angular momentum ± 2, optically forbidden) and bright states (total angular momentum ± 1, optically allowed). Thus we have to consider two radiative transition rates with $\Gamma_{\mathrm{rad}}^{\mathrm{bright}} \gg \Gamma_{\mathrm{rad}}^{\mathrm{dark}}$; (ii) the bright $|\pm 1\rangle$-dark-$|\pm 2\rangle$ state splitting depends on the confinement potential and may vary between 0.1 and 15 meV [56–60]. A thermal population of the bright state $|\pm 1\rangle$ from the dark state $|\pm 2\rangle$ with the rate γ_{th} is possible which results in the temperature dependence of the observed decay behaviour [61, 62]; (iii) efficient trap processes can cause fast initial decay components, unless the traps become saturated or have negligible concentrations; (iv) in QD ensembles, energy transfer processes with rates γ^{ET} can contribute to the bright and dark state population. Photons emitted by smaller QDs can be absorbed by larger QDs or energy can directly be transferred via Förster-energy transfer [63]. The energy transfer processes have been added in the left scheme, as examples, by the rates γ^{ET}; and (v) asymmetries in the dot shape or confining potentials result in additional fine structure of the confined electron–hole pair ground and excited states.

In nanocrystals and epitaxially grown islands, a different way of labelling the fine structure has been established in the literature, although the underlying physics causing the splittings is the same exchange interaction. For example, in nanocrystals, five exciton states were considered in [56, 57], produced by the exchange interaction and non-spherical shape (not shown in the left part of Fig. 8). The five levels are assigned to the angular momentum projection ± 2, $\pm 1^L$, 0^L, $\pm 1^U$, 0^U, where U and L denote upper and lower states with the same projection. Transitions between the crystal ground state to states with ± 2 and 0^L are dipole forbidden, while transitions to states $\pm 1^L$, $\pm 1^U$, and 0^U are dipole allowed. The states lowest in energy are those with the labels ± 2 and $\pm 1^L$ which are plotted in the left scheme as dark $|\pm 2\rangle$ and bright $|\pm 1\rangle$ states. The bright–dark splitting energies in CdSe nanocrystals vary between 1 and 15 meV for sizes between $3\,\mathrm{nm} < R < 1.5\,\mathrm{nm}$. At low temperature, thermal activation is only discussed for the $|\pm 2\rangle$ to $|\pm 1\rangle$ transition because of the large energy separation calculated for the transition to the higher dipole-allowed states $\pm 1^U$ and 0^U. The thermal refilling rates γ_{th} cause the complex temperature dependence of the decay times.

The usual classification of the fine structure levels in epitaxially grown CdSe QDs is sketched in the right part of Fig. 8. In anisotropic CdSe islands embedded in a wide-bandgap quantum well, the exchange interaction splits the heavy-hole exciton state likewise into a bright state $|\pm 1\rangle$ and a dark state $|\pm 2\rangle$ classified by a splitting energy δ_0 according to [60]. For QDs of cylindrical symmetry (point group symmetry $\mathrm{D_{2d}}$), however, the dark state is split further by a splitting energy δ_2 into a doublet. Further symmetry lowering splits the bright state by a splitting energy δ_1 into two states which recombine to the ground state by emitting linearly polarized light. Since the splitting energy δ_0 is again only a few meV, a thermal refilling with γ_{th} of the bright state $|\pm 1\rangle$ from the dark state $|\pm 2\rangle$ with increasing temperature is possible, resulting again in the temperature dependence of the decay behavior [62].

The main differences in the recombination dynamics of CdSe nanocrystals and epitaxially grown CdSe islands em-

bedded in ZnSe quantum wells are: (i) The creation of electron hole–pairs proceeds via two different absorption processes. In nanocrystals, the absorption process is only possible into excited states of the quantum dot itself and governed by the nanocrystal absorption cross section. In epitaxially grown islands the pump is usually resonant to the quantum well absorption, i.e. resonant to a two-dimensional (2D) nanostructure with a high density of absorbing states. (ii) In epitaxially grown CdSe islands it is assumed that the energy separation with respect to the next higher state in energy is much smaller than in nanocrystals. Thermal escape into these states, originating either from the next higher confined QD state, from fine structure splittings or from the surrounding QW, is no longer negligible. (iii) The presence of additional charges or charge fluctuations seems to influence the nanocrystal dynamics [64], also evidenced by the observation of blinking, spectral wandering and similar phenomena. Charged excitons (trions) or excitons bound to charged traps (donor-bound excitons) represent an additional channel which can be thermally activated and contributes then to a decay time similar to the exciton decay, resulting also in temperature-dependent dynamics. Such a channel is introduced as γ_t in the left decay scheme for nanocrystals. In epitaxially grown islands such a process might also be present, but is probably less important because of the more efficient population of the bright state via the quantum well population. (iv) In epitaxially grown islands, the present density of the quantum dots is not high enough to enable Förster-energy transfer processes. The scheme in the right part of Fig. 8 is a typical single-dot scheme, usually applied in case of CdSe islands.

The scheme of Fig. 8 describes experiments under low excitation conditions, i.e. the number of electron–hole pairs per nanocrystal is assumed to be well below one and effects of multiple electron–hole pair populations are neglected. Recently, the nanocrystal absorption cross section was successfully determined in [65, 66] to be $\sigma \sim 10^{-15}\,\mathrm{cm}^2$. Therefore, the experimental conditions can easily be adjusted to maintain the low-excitation limit in the excitation intensity.

From the above discussion we can derive an optimum nanocrystal type suitable for experiments aimed at the modification of the radiative transition rates via coupling to the optical modes of a microcavity (see Sect. 4.2). For these experiments we have to select CdSe nanocrystals with larger sizes (smaller bright–dark splitting) and work at temperatures for which the thermal energy is large enough to ensure a sufficient population of the bright state. Under such conditions, the measured dynamics should be most sensitive to the change of the radiative decay rate $\Gamma_{\mathrm{rad}}^{\mathrm{bright}}$ of the bright state. We have to avoid the fast initial decay due to population of traps by careful synthesis of CdSe/ZnS core/shell nanocrystals. Since we work with ensembles of quantum dots, we have to take into account the energy transfer from smaller to larger QDs, which can be done by choosing an appropriate detection energy. This is illustrated in Fig. 9, which shows the variation in the decay characteristics within the inhomogeneously broadened emission band of the CdSe nanocrystals used for our experiments. The decay times have been determined for different spectral positions taken within the inhomogeneously broadened PL band of CdSe nanocrystals with a center wavelength of 615 nm at $T = 5$ K. Fast initial decay constants are observed at the high-energy side of the PL-band, i.e. energy relaxation from excited quantum dot states to ground states of the same or another dot can take place. The PL-dynamics at higher energy are characterized by a two-component decay, while detection at the low-energy side does not show the fast initial component. Because of the fast time constants of the initial decay component in the ~ 100 ps range, we cannot unambiguously assign the energy transfer to a Förster-type process [63]. More probably, it is a photon-mediated emission/reabsorption process, but further studies are required to clarify this question. At energies below 2.0 eV, the fast initial decay becomes negligible and the overall decay approaches a single time constant of a few nanoseconds.

The slow decay component found at all detection energies is a few nanoseconds, indicating a decay channel dominated

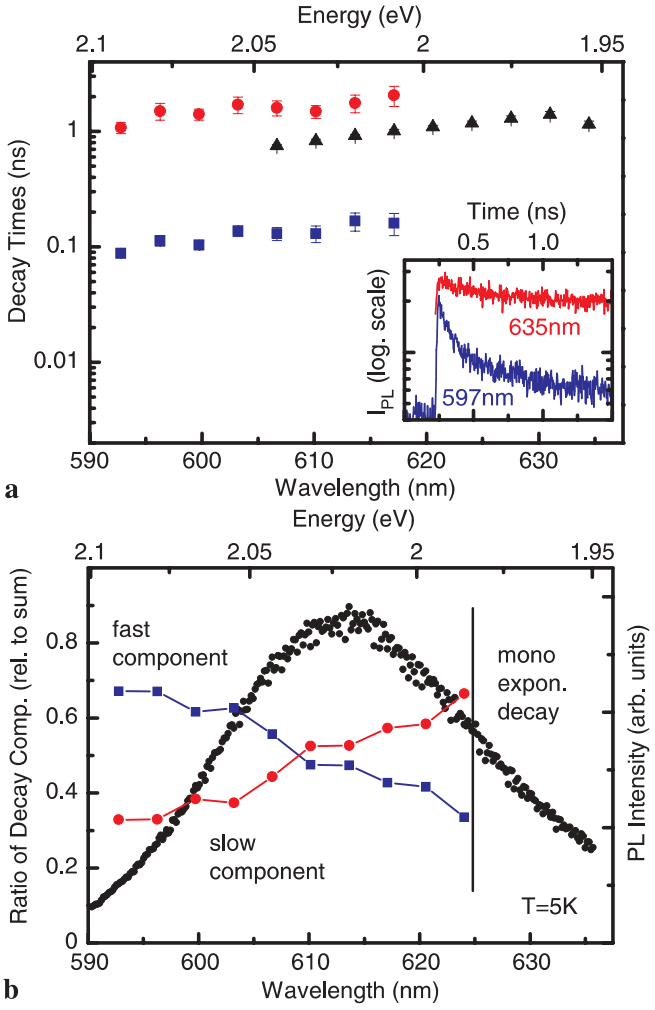

FIGURE 9 **a** Decay times derived for different spectral positions within the inhomogeneously broadened PL band of CdSe nanocrystals with a center wavelength of 615 nm at $T = 5$ K. The decay curves at the high-energy side are characterized by fast initial decays due to energy transfer and are fitted by a bi-exponential function (red and blue symbols), while the decay at the low-energy side is described by an almost monoexponential nanosecond decay time (*black symbols*, compare also the *inset*). **b** Ratio of the slow and fast components relative to the sum determined for different spectral positions within the PL band of the CdSe nanocrystals (*black symbols*). At energies below 2.0 eV, the fast initial decay is small and the overall decay approaches a single time constant in the nanosecond range

by $\Gamma_{\mathrm{rad}}^{\mathrm{bright}}$. In the literature, experiments which are aimed at the determination of the radiative lifetime for the optically allowed transition under optimum elimination of non-radiative trapping processes, report times in a range between 1 ns and 30 ns for $\Gamma_{\mathrm{rad}}^{\mathrm{bright}}$ and nanocrystal sizes between $R = 1.8$ nm and $R = 4$ nm [61, 64, 67] at low temperature. A $\Gamma_{\mathrm{rad}}^{\mathrm{bright}}$ of several or tens of nanoseconds has been also observed in photon anti-bunching experiments in [65].

3.3 *Emission of single nanocrystals*

Spectral diffusion and fluorescence intermittency (blinking with "on–off" behavior) are long-debated features for wet-chemically prepared single nanocrystals [64, 68–71]. Based on the observed power laws of the on- and off-time probabilities and the detailed kinetics of the fluorescence intermittency, different mechanisms like the quantum-jump model, Auger ionization, thermally activated kinetics, hopping and tunnelling, and fluctuating electronic and/or structural environments of individual nanocrystals are presently discussed (see [71] and Refs. therein). A simple model to explain blinking of QDs is based on the idea that the charge state of a quantum dot may change due to carrier escape. The simultaneous changes in the surrounding local electric fields result in correlations between intensity fluctuations and spectral diffusion.

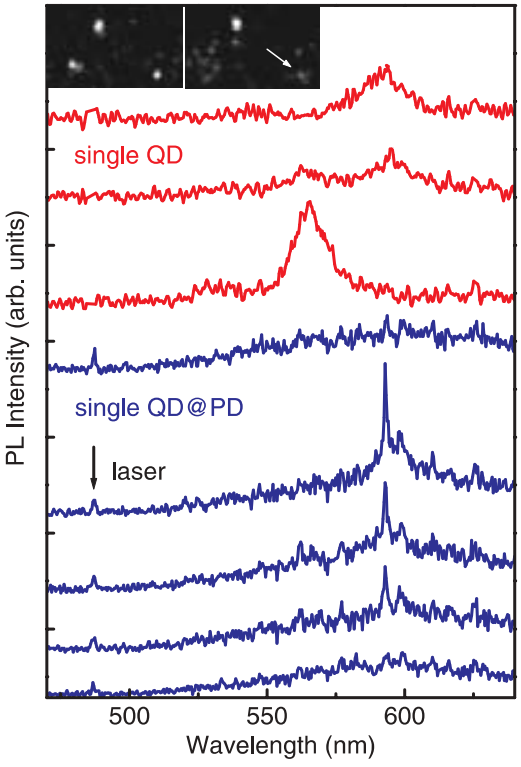

FIGURE 10 Room-temperature emission spectrum of single CdSe QDs: *Red curves* show single CdSe nanocrystals, without cavity, taken at different observation times, to illustrate the blinking effect associated with spectral diffusion in nanocrystals. *Blue curves* show the same experiment for a single QD but now bound to a PD. The emission of the QD switches two very sharp modes of high Q (mode width below spectral resolution). The signal from the scattered laser light is shown too, to exclude any correlation with fluctuations in pump intensity. The spectra are recorded 2 s apart

To demonstrate the possibility of coupling only a single QD to a single cavity mode, we may exploit the effect of photoluminescence-blinking from single nanocrystals. Beside photon correlation techniques such as anti-bunching experiments [65, 72], the finding of blinking may serve as a good indication of a pure single-dot emission. In a single microsphere containing only a single CdSe QD, the QD should switch single modes "on" and "off" according to its blinking frequency. This is illustrated in Fig. 10, which shows the blinking for a QD on a glass microsphere (QD@PD) compared to a single QD without cavity recorded at room temperature. The emission of the quantum dot switches two very sharp modes of high Q. In the process of spectral diffusion, the cavity might act as a spectral filter, which allows only the observation of nanocrystals without spectral jumps or with spectral shifts equal to the cavity mode separation [73].

3.4 *Homogeneous line broadening*

Temperature-dependent single-dot emission spectroscopy and spectral hole burning are the most widely used experimental methods for studying homogeneous line broadening in nanocrystals. The analysis of line shapes in single-dot emission is complicated by the problem of spectral diffusion and power broadening. A strong dependence of single-dot line widths on excitation intensity, wavelength, temperature and integration time is found [68–70]. The low-temperature line widths observed in PL spectra are of the order of 100 μeV. Because the reported values are often resolution limited, they can be considered as an upper limit for the actual homogeneous line broadening. High-resolution spectral hole-burning has been applied in [74, 75] and a zero-phonon line width (FWHM) as narrow as 6 μeV has been measured in wet-chemically prepared CdSe/ZnS core/shell nanocrystals at $T = 2$ K. The temperature dependence of the homogeneous line width has been investigated by means of accumulated photon echo techniques at very low temperatures down to 0.6 K [76]. The Fourier-cosine transform of bi-exponential decays in the accumulated photon echo signal yields a narrow Lorentzian superimposed on a broader background band. At very low temperature the line-broadening mechanism is assigned to the interaction with confined acoustic phonons [59, 74, 77]. For the CdSe/ZnS core/shell nanocrystals used in our experiments, room-temperature single-dot spectroscopy reveals PL bands of ~ 60 meV [73]. At $T < 20$ K the single-dot PL line width drops below 200 μeV (see Fig. 14 in Sect. 4.2), i.e.,for our microcavities, the condition of similar quantum dot and cavity line widths can be fulfilled in a temperature range $T < 20$ K.

4 Quantum Dots in Photonic Dots

4.1 *Preparation and optical characterization*

In the literature one can find reports about CdSe nanocrystals as active optical emitters in planar optical cavities [78, 79] and three-dimensional (spherical) optical cavities [2, 42, 61, 73, 80] consisting of micrometer-sized polymeric, glass or fused-silica spheres. Different methods have been tested by us to optimize both the Q-factor and emitter position/orientation. All microspheres used had sizes

between $1.5\,\mu\text{m} < R < 6\,\mu\text{m}$, a good compromise between high Q and small mode volume. The first type of quantum dot in a photonic dot structure realized in our investigations was a monolithic polymeric (PMMA) microsphere, homogeneously doped with (CdSe)ZnS core/shell nanocrystals [2]. This was followed by hollow microspheres [42]. Commercially available glass microspheres, usually produced via fast melting of fine monodisperse glass powder in the flame flow and subsequent solidification, are also used as a nanocrystal template because of their nearly perfect sphericity and surface smoothness, as the result of the surface tension in a liquid glass microdroplet. The chemical attachment of nanocrystals to the glass surface was achieved by using bifunctional molecules, like mercaptopropyltrimethoxysilane (MPTS) [73]. A prolonged treatment of glass microspheres in a water-free MPTS solution results in the formation of a MPTS monolayer via Si–O–Si chemical bonds between MPTS silane groups and the glass SiO_2 cage. The MPTS mercaptogroups remain free for further attachment of (CdSe)ZnS core/shell nanocrystals via Zn–S bonds. The Q factor of glass microspheres routinely exceeds 10 000. Since the loading of glass microspheres with high concentrations of CdSe nanocrystals is difficult to achieve, we utilized commercially available polystyrene microspheres with very high $Q \sim 10\,000$ for experiments with high nanocrystal concentrations. Polystyrene (PS) easily dissolves in chloroform and other chloroorganic solvents, but not in alcohols. In an appropriate mixture of chloroform and 2-propanol (ca. 1 : 10 v/v), the outer shell of PS microspheres partially swells and the nanocrystals may penetrate the surface of the microsphere from the solution. Subsequent removal of the solvent results in the capture of nanocrystals inside the subsurface region of the microspheres, where the coupling of nanocrystal emission to cavity modes with radial quantum number $n = 1$ is maximum. This "penetration" method is suitable for impregnation of PS microspheres either by nanodots or nanorods. The nanorods may also be attached to the surface of a PS microsphere by an electrostatic method. This method is based on the electrostatic interaction between the negatively charged surface of PS microspheres and positively charged nanorods or nanodots. Most of the commercially available pure PS microspheres with no special functional surface groups exhibit a strong surface negative charge in the solution due to presence of surface sulfate groups. In order to make nanorods or nanodots highly positively charged, the stabilizing layer of TOPO/HDA molecules on the surface of the nanocrystals is replaced by 2-(dimethylamino)ethanethiol hydrochloride. The nanocrystals are very soluble in water and strongly adhere to the surface of the negatively charged PS microspheres. Such a preparation results in a tangential alignment of nanorods with respect to the microsphere surface (see Sect. 4.3).

The optical characterization has been performed by applying imaging spectroscopy at the diffraction limit, combined with a polarization-sensitive mode-mapping method and comparative mode calculations based on standard Mie theory and the semi-analytical multiple-multipole technique. The emission of QD-doped spheres is spectrally and spatially resolved by mapping the intensity across a sphere on and off resonance to cavity modes for a fixed polarization plane (see

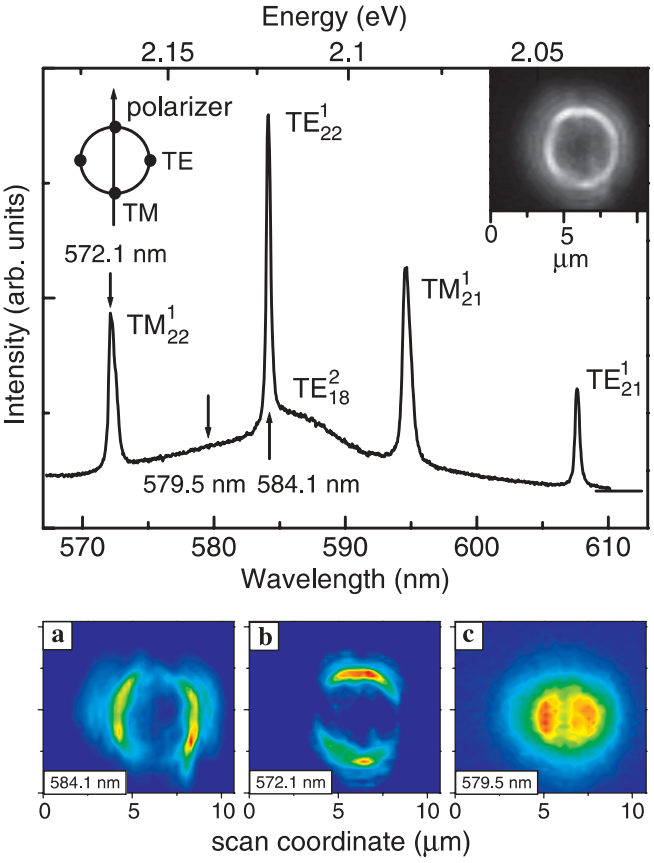

FIGURE 11 Measured spectrum of CdSe QDs bound to the surface of a $R = 1.8\,\mu\text{m}$ microsphere ($\lambda_{\text{exc}} = 488$ nm, $T = 300$ K, $I_{\text{exc}} = 20\,\text{W/cm}^2$). The mode quantum numbers are assigned using Mie theory. The *right inset* shows the microscopic image of the microsphere, spectrally resolved at the TE^1_{22}-resonance (unpolarized detection). The *left inset* shows the polarizer orientation, for which the mode mapping is performed at 572.1 nm (TM^1_{22}), 584.1 nm (TE^1_{22}) and 579.5 nm (*background*). The *lower part* shows the two-dimensional intensity scans (**a**–**c**) for the spectral positions indicated by *arrows* in the spectrum

Fig. 11). A polarizer inserted into the optical beam path in front of the detection system selects only signals from QDs which emit components of the electromagnetic field parallel to the orientation of the polarizer. For a fixed polarizer orientation parallel to the z-axis, the TE modes should appear as bright spots in the equatorial plane whereas the TM modes have their main intensity perpendicular to the TE modes and form spots at the poles (for details see [43]). The experimental concept of polarization-sensitive mode mapping represents a convenient tool for determining the polarization properties, in particular for larger microspheres, without performing extensive numerical calculations.

In Figs. 12 and 13 we give an overview of the typical spherical microcavities used in our experiments. Figure 12 shows the emission spectrum for a single, hollow microcavity excited by the 488nm-line of an Ar^+-laser. The doping of the polymer PMMA (poly-methylmethacrylate) with CdSe QDs is described in [2, 42]. The most important advantage of hollow spheres, as compared to bulk spheres, is the controlled arrangement and fixation of the light-emitting dipoles close to the surface of the microcavity. To evidence the origin of the observed peaks from a 3D-cavity effect, the mode

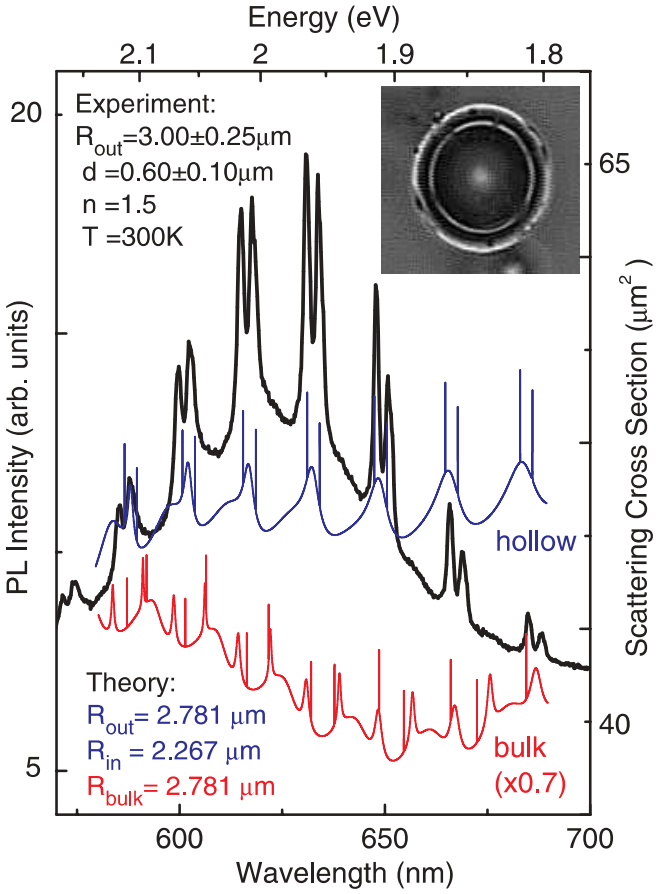

FIGURE 12 Room-temperature emission spectrum of a single, hollow microsphere of $R_{out} = 3 \pm 0.25$ μm outer radius and $d = 0.6 \pm 0.1$ μm shell thickness, excited by an Ar^+-ion laser and measured by use of a $20\times/0.4$ NA microscope objective, an imaging spectrometer and a CCD-camera. For comparison, the calculated cross section of light scattering is shown for a hollow PMMA sphere of $R_{out} = 2.781$ μm, $R_{in} = 2.267$ μm and $n = 1.5$ (*blue*), and for a bulk PMMA sphere of the same size (*red*). The *inset* shows a typical microscope image of a hollow polymer microsphere

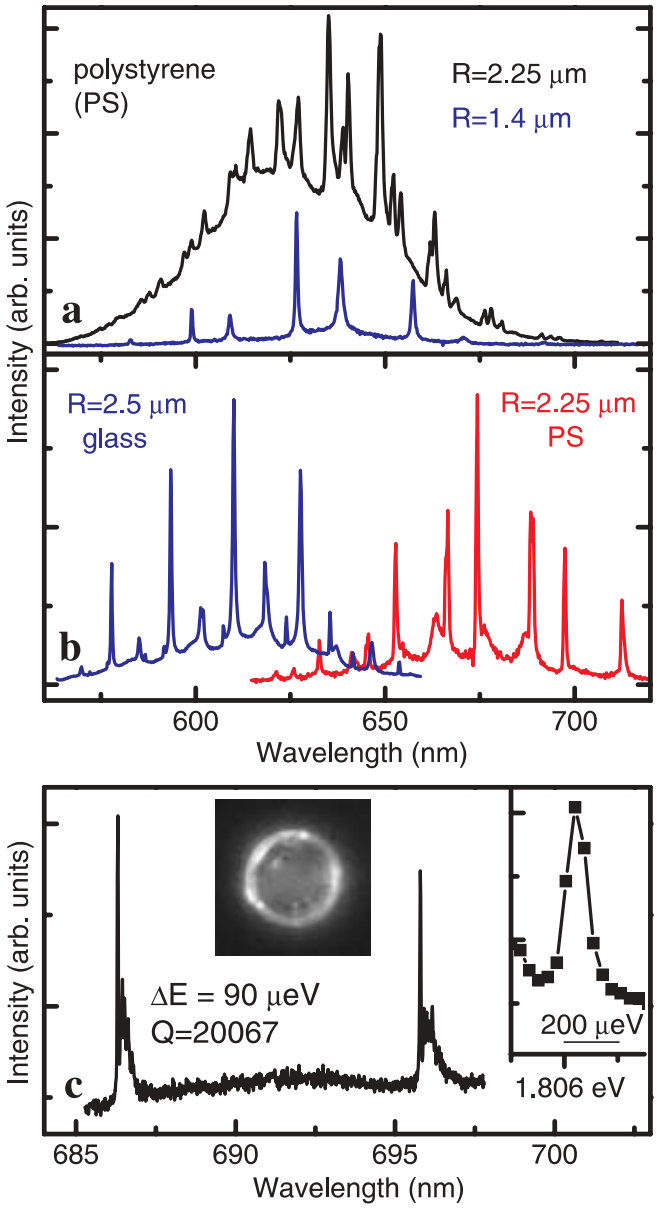

FIGURE 13 **a** Emission spectra of a $R = 2.25$ μm microsphere covered by a high concentration of CdSe quantum dots (*black*) and a $R = 1.4$ μm microsphere covered by a low QD-concentration (*blue*), **b** Emission spectra for two different CdSe nanocrystals: dots with $R_{QD} = 2.5$ nm (*blue*) and rods with $R_{QR} = 3.5$ nm and 35 nm in length (*red*) covered to a glass and polymer microsphere of similar radius R, **c** The spectrum shows the highest quality factor Q measured for a $R = 2.5$ μm glass microsphere surface-impregnated with CdSe quantum dots. The spectral resolution is 20 μeV. All spectra were taken at $T = 300$ K

spectrum has been calculated for the parameter of the hollow cavity and compared with the experiment, as shown in Fig. 12. Good agreement is obtained for a hollow sphere with $R_{out} = 2.781$ μm, $R_{in} = 2.268$ μm (outer and inner radii), and $n = 1.5$ for the index of refraction of the QD-doped polymer ($n = 1.0$ for air inside and outside the hollow sphere). The mode separation is very sensitive to the shell thickness d and cannot be reproduced by fitting the spectra by a bulk sphere of same R_{out}. The theoretical spectra of the confined microcavity states predict spectrally well-separated high-Q modes (up to 10^5) for the radial quantum number $n = 1$. The experimentally obtained spectrum shows that the radiation emitted by the CdSe QDs excites predominantly the cavity modes of highest Q formed by those $n = 1$ modes, which have a single maximum in electromagnetic energy density close to the surface, just at the position of the QDs. Q values between 2000 and 4000 can easily be achieved in the prepared microspheres.

Beside the fabrication of self-made hollow microspheres with only moderate values of Q, another route for preparing microsphere cavities with $Q \geq 10^4$ values is the surface coverage of commercially available polymeric and glass microspheres with very high surface quality material with high transparency and sphericity. By varying the nanocrystal concentration, both high- and low-loaded microspheres can be prepared with radii in the range between 1.5 μm and 10 μm. Figure 13a shows spectra of polymer microspheres (Polystyrene (PS)) of two different sizes surface-impregnated with CdSe nanocrystals in two different concentrations: a small $R = 1.4$ μm sphere loaded with a low concentration of CdSe QDs and a larger, $R = 2.25$ μm sphere doped with a very high concentration of CdSe QDs. The typical features one can find are: (i) in the case of a high CdSe concentration, a stronger background emission and stronger mode damping in the spec-

tral range overlapping with the absorption spectrum, while at low CdSe concentration the absorption is negligible and almost no background is seen; and (ii) a large free spectral range of about 15 nm between adjacent modes in case of small spheres while the mode number increases rapidly for larger radii. In both spectra of Fig. 13a the same size of CdSe QD's is used ($R_{QD} = 2.5$ nm), i.e. the envelope of the cavity mode spectrum is given by the ensemble PL spectrum of the QDs. The Q values are higher for the larger spheres ($4000 < Q < 8000$) but can still be as large as $Q \sim 1000$ for the smallest spheres of $R \approx 2\lambda$. In our experiments, small polymer and glass microspheres with similar refractive index n yield comparable Q values.

With Fig. 13b, we illustrate how the cavity emission can be spectrally tuned over a spectral range between 550 nm and 725 nm using different types of CdSe nanocrystals. Through implementation of other types of II–VI nanocrystals, like ZnSe, CdTe and PbSe, the spectral range may be extended from the UV to the near-IR region. Thus, semiconductor quantum dots are very attractive nanoemitters for microcavity applications. In Fig. 13c, we show an example of the highest Q value we could achieve in our samples. A value of $Q \sim 20000$ is measured for a $R = 2.5$ μm glass sphere surface covered with a very low concentration of CdSe nanocrystals. Since the cavity Q factor is directly related to the lifetime of the photon in the cavity, we can estimate here a time constant $\tau_{cav} \approx 10$ ps, i.e. in low-Q modes light decays quickly while narrow, high-Q modes retain light longer.

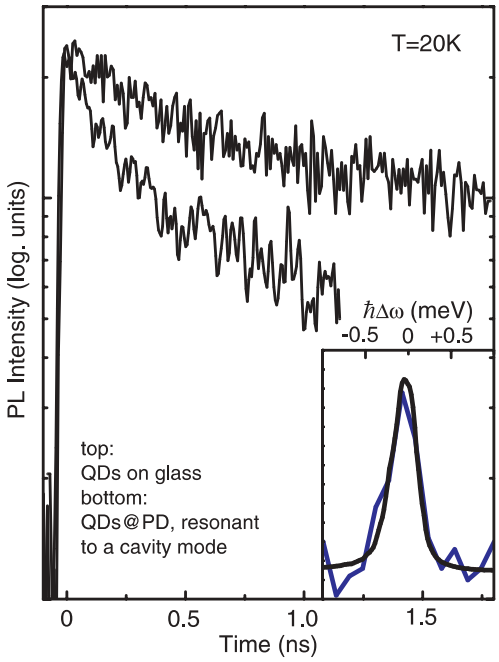

FIGURE 14 Modification of photoluminescence decay measured for optimum experimental conditions, i.e. detection in the low-energy tail of the ensemble emission of $R_{QD} \sim 2.5$ nm CdSe nanocrystals resonant to a $Q \sim 7500$ cavity mode (bottom) and compared with CdSe nanocrystals prepared by the same chemical process, but deposited on a glass substrate (*top*). $T = 20$ K, $\lambda_{det} = 586.7$ nm, excitation by a 120-fs pulse at 445 nm (frequency-doubled Ti:Sa laser), detection spatially, spectrally and temporally resolved using a microscope objective (spatial resolution 0.5 μm), an imaging spectrometer (spectral resolution 0.1 nm), and a streak camera (time resolution 20 ps). *Inset*: Spectral line widths at $T = 20$ K measured in a separate experiment with highest spectral resolution for a representative single CdSe QD (*blue*) and a representative PD mode (*black*)

4.2 *Purcell-Effect*

The studies of the quantum dot–electromagnetic field interaction in cavities and of modified spontaneous emission constitute the growing field of cavity quantum electrodynamics based on semiconductors. The inhibition and enhancement of the spontaneous emission, i.e. the search for the Purcell effect in semiconductors (see Sect. 1), is studied for III–V quantum dots in epitaxially grown microstructures [81–83] and CdSe nanocrystals in three-dimensional microcavities (glass or polymeric microspheres) [61, 73]. Illustratively speaking, the Purcell effect is a typical phenomenon observed in the weak quantum dot–cavity coupling regime: the spontaneous emission is still dominant over induced emission due to the self-emitted field, but modified by the modified density of photon states as a result of photon confinement in the microcavity.

As has been discussed in the previous Sections, the experimental proof of the Purcell effect is confronted with several experimental obstacles, such as the background from emission in higher radial modes, the strong decrease in signal when the wavelength is tuned out of cavity resonances, the size-, intensity-, energy- and surface trap-dependent decay of the quantum dot emission, the temperature-dependence of both dark–bright splitting and homogeneous linewidths of the quantum dots, etc. In our experiments, we compared the luminescence decay at low temperature at wavelengths resonant to cavity modes for different glass microspheres (R between 2 μm and 4 μm) and for nanocrystals prepared under the same chemical conditions, but deposited on glass substrates. We avoided the effects of high excitation density by measuring first the power-dependent decay times to derive the low-density limit experimentally in order to ensure that the excited number of electron–hole pairs per nanocrystal was less than one. The observed changes in lifetime varied by a factor of two to five, depending on the cavity mode Q-factor, and the size of the nanocrystals (selected by the detection energy).

Representative luminescence decays are shown in Fig. 14. The most pronounced modification of the measured photoluminescence decay rates is found by selecting optimum experimental conditions: the almost monoexponential decay without a cavity (1.2 ns) is modified in resonance with a cavity mode (220 ps) by a factor of approximately five. A temperature of $T = 20$ K was chosen in the experiment in order to adjust the homogeneous line broadening of the single QD to a value equal or smaller than the cavity mode width (see inset of Fig. 14. Since the time-averaged spectrum of a single QD is influenced by spectral wandering, we expect even smaller homogeneous broadenings for shorter integration times). The cavity-induced enhancement in the photoluminescence decay rate was observed in particular for larger nanocrystals with negligible exchange splitting of the lowest electron–hole pair state [73].

4.3 *Nanorod orientation and β-factor*

In Sect. 2 we discussed how the excitation of cavity states depends on the orientation of the dipole, i.e. here the

CdSe nanorod axes (Figs. 3 and 4). Thus, an active polarization control and an efficient coupling of spontaneous emission into cavity modes is feasible if the properties of the photon-emitting species in the cavity can be designed by engineering the orientation of the optical transition dipole moment. In this Section we demonstrate the concept of aligned semiconductor nanorods to achieve high coupling coefficients β of spontaneously emitted photons into microcavity modes. The preparation and optical properties of the nanorods used are described in Sect. 3. We apply here the wet-chemical preparation method for CdSe nanorods described in [52, 55, 84], allowing us to use them for controlling the microsphere emission by the engineering of nanorod orientation.

We impregnated polymeric microspheres of $R = 1.4\,\mu\text{m}$ radius specifically with nanorods using two methods: (i) an electrostatic attachment method which results in a single monolayer of tangentially aligned nanorods on the sphere surface and (ii) a subsurface impregnation which gives a higher concentration of less perfectly oriented nanorods. The control of the cavity mode polarization by nanorod alignment was examined by comparing the cavity emission of microspheres of similar size measured under identical experimental conditions, but doped either with almost isotropic CdSe nanodots or anisotropic CdSe nanorods. The cavity mode polarization was determined experimentally using the polarization-sensitive mode mapping described in Sect. 4.1 and [43]. Figure 15b shows the cavity spectrum for CdSe quantum dots positioned in a thin subsurface layer, ensuring low losses and resulting in $Q = \hbar\omega/\Delta\hbar\omega$ values of about 1000 for the small $R = 2\lambda$ cavity. For quantum dots, the full cavity mode spectrum was observed with peak intensities given by the envelope of the ensemble emission. Figure 15a shows the spectrum for the same microsphere size, but now with tangentially aligned CdSe nanorods prepared by method (i). As can be clearly seen, the TM-mode intensity is drastically reduced, as predicted from the discussion of Fig. 3. Still, the spacer molecule used in the preparation method (i) causes losses in the coupling efficiency, which result in a PL background (subtracted in Fig. 15b) and somewhat smaller Q values between 300 and 600. The tangential nanorod alignment results in efficient excitation of the transverse electric field modes, while transverse magnetic modes are suppressed, and an active control of the mode spectrum is achieved in this way [85].

The more efficient excitation of TE cavity polarization states by tangentially aligned CdSe nanorods is likewise evidenced in the pump power dependence of the microcavity emission, shown in Fig. 16. The nanorod alignment results in a non-linear increase in TE-mode intensities and in a very efficient coupling of spontaneous emission into solely TE modes. At highest pump power the spectrum is dominated by only two TE-polarized modes.

The analysis of such intensity characteristics as shown in Fig. 16 opens a way to a more detailed understanding of such cavity parameters as photon occupation numbers or threshold intensities. Presently, however, such experiments are faced with the problem of photodegradation. In an attempt to overcome this problem, pulsed excitation and thick, close-packed nanorod layers were employed recently [86]. Based on our results from both dots and rods, we consider CdSe nanorods as one of the most photostable nanoemitters. In particular,

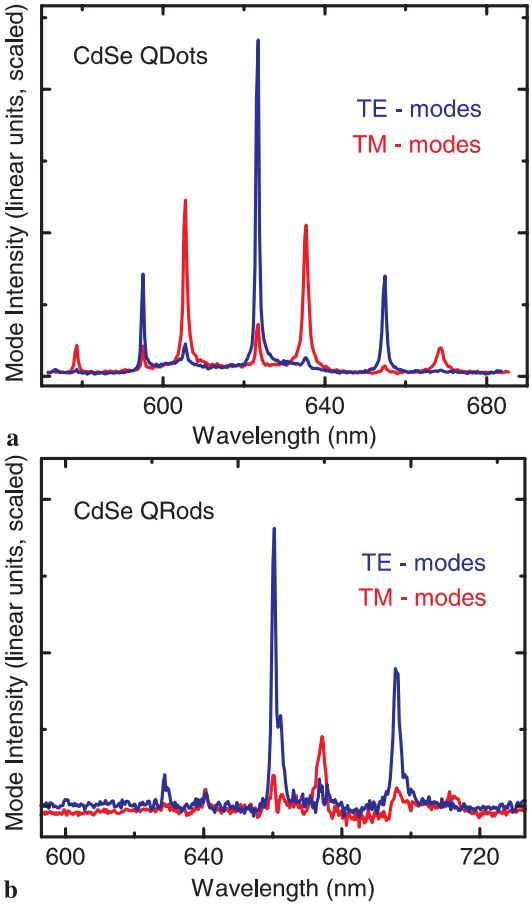

FIGURE 15 Control of the cavity photon polarization by oriented nanorods: **a** Microsphere spectrum ($R = 1.4\,\mu\text{m}$) excited by CdSe quantum dots showing the full set of cavity modes represented by the sum of the two subsets of TE (*blue*) and TM (*red*) mode spectra. The peak heights of the corresponding TE and TM modes are determined by the envelope spectrum of the ensemble emission. **b** The same for CdSe nanorods, showing pronounced TE cavity modes and almost complete suppression of TM modes. $T = 300\,\text{K}$. Excitation at 488 nm

we expect in low-temperature experiments a conservation of the number of active nanoemitters, allowing us in future to make an exact measurement of the intensity-dependent input/output characteristics to infer further important microcavity parameters, such as the so-called β value characterizing the coupling coefficient of spontaneous emission into a cavity mode. Microcavities which allow one to bring the mean cavity photon number close to unity are attractive research objects for investigating the threshold-less laser, as proposed in [87]. The best β values for II–VI-based microcavities have been reported for planar cavities with $\beta \sim 10^{-2}$ [88]. With a simple rate-equation system, such as that presented, for example, in [89], we have calculated the cavity photon number as a function of pump power using a parameter set appropriate to our quantum dot/microsphere system. Figure 17 shows for a fixed nanocrystal number of $N_0 = 10^4$ in resonance with a cavity mode the corresponding curves with β as the parameter. The chosen N_0 corresponds to a standard preparation route yielding a monolayer of uncoupled nanocrystals covering the sphere surface. As can be seen, for low β values, the typical threshold behavior can be realized if sufficiently high pump power is applied. Such threshold characteristics have been re-

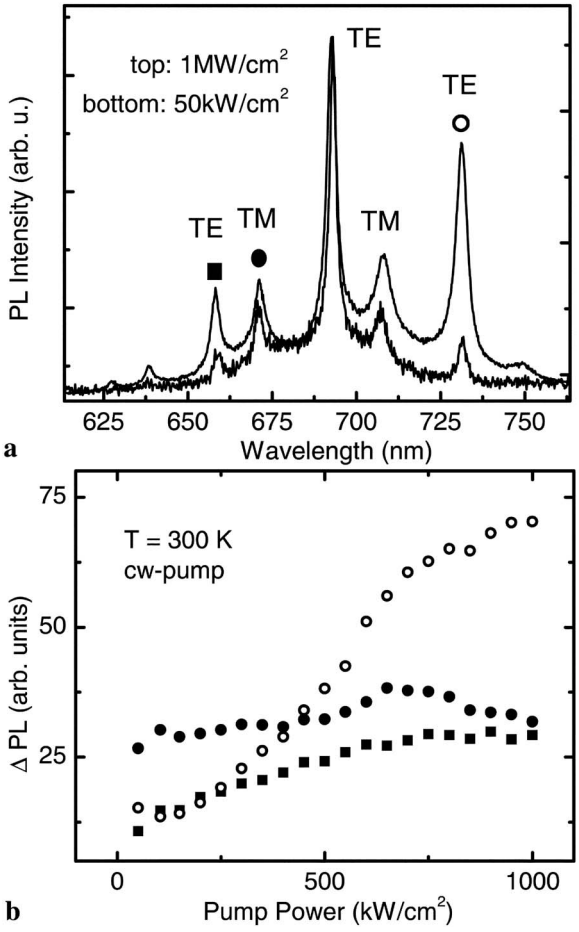

FIGURE 16 The change in TE mode intensities with increasing cw pump power: **a** Two spectra at low and high pump power normalized with respect to the central TE mode intensity at 693 nm. **b** Pump-power dependent difference ΔPL of the mode under consideration (*full circles* – TM mode at 671 nm, *open circles* – TE mode at 731 nm, *squares* – TE mode at 657 nm) with respect to the central mode at 693 nm. $T = 300$ K, excitation at 488 nm

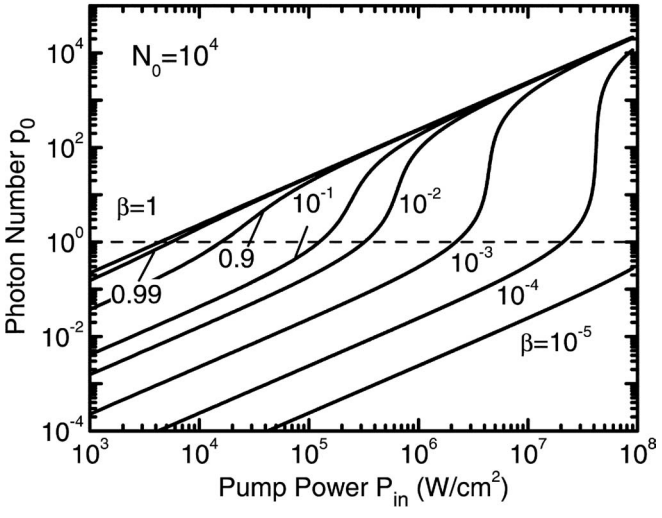

FIGURE 17 Coupling coefficient β of spontaneous emission into a cavity mode calculated for a parameter appropriate for describing CdSe quantum dots coupled to a $R = 2.5\,\mu$m microsphere: $\sigma = 4 \times 10^{-16}\,\mathrm{cm}^2$ for the quantum dot absorption cross section, $N_0 = 10^4$ for the number of nanocrystals resonant to a single cavity mode, 300 μeV for the cavity mode width, $\tau_{rad} = 2$ ns and $\tau_{nr} = 1\,\mu$s for the radiative and non-radiative decay times. The *dashed line* characterizes the threshold at which the mean cavity photon number is unity

ported for low-Q microcavities loaded with nanocrystals of high concentration under pulsed excitation [73, 79, 86]. The transition to threshold-less input–outpout characteristics has not been demonstrated yet. While theoretical estimates for quantum dot/sphere systems are promising [90], the major experimental problem consists of the development of suitable photon detection techniques, which allow measurement of the photon number p_0 and its statistics accurately, and the problem of nanocrystal degradation resulting in a non-constant N_0.

5 Outlook

Experimental results for the weak coupling regime have been obtained, but the experimental observation of strong coupling is still not reported yet. It turns out that we have to solve a complex optimization problem, both for cavity and quantum dot parameters [7, 14]. The cavity should show a large ratio Q/V, i.e. large Q and small mode volume V, a requirement, however, which can not be fulfilled simultaneously and has thus to be optimized. Our microsphere with radii between 2 μm and 3 μm showed cavity mode widths of 100 μeV, which is of the order of the calculated vacuum Rabi splitting energy for CdSe quantum dots (Fig. 18). The Rabi splitting energy has been estimated here taking into account the refractive index difference between semiconductor and glass or polymer according to [91]. The observation of mode splitting has been reported; however, it has to be clarified that the splitting is not caused by sphere asphericities etc. The nanocrystalline system can be engineered by optimizing the exchange splitting, i.e. the energy difference between bright and dark states. The shape variation also implies an engineering of optical transition dipole moments (and permanent dipole moments as well). We expect that a radiative decay time variation within a factor of ten should be possible. The analysis of the photon statistics for the emitted photons, the control of position and concentration of the nanoscopic emitters, the combination of concepts developed for microspheres with other types of three-dimensional microcavities are inter-

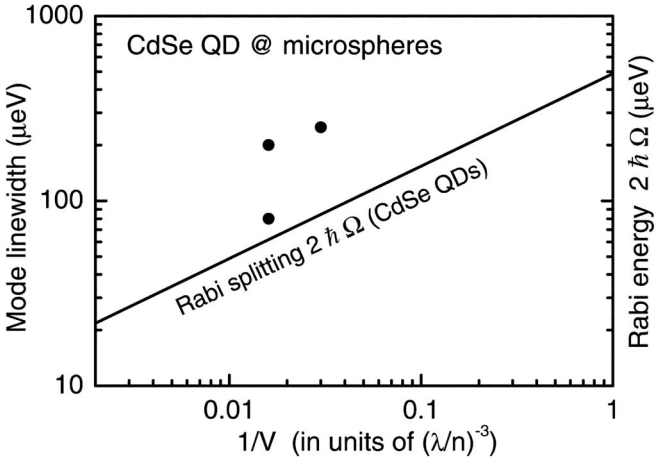

FIGURE 18 The calculated Rabi splitting energy for CdSe quantum dots plotted as a function of the inverse effective cavity volume $1/V$ in units of $(\lambda/n)^{-3}$, compared to the experimental mode linewidths measured for the microsphere cavities studied here. For the radiative lifetime of the CdSe nanocrystals 1 ns is assumed, and an emission wavelength at 550 nm

esting tasks for future research. The nanocrystal/microsphere system is a cheap and excellent model system to learn about cavity quantum electrodynamics with semiconductor quantum dots, and many results can be generalized to other semiconductor-based microcavities.

ACKNOWLEDGEMENTS We thank C. Ell, W. Langbein and H.J. Weber for helpful discussions and experimental support, and D. Klimov from the Shemyakin-Ovchinnikov Institute (Moscow) for providing us with the TEM pictures. Financial support of the DFG, Grant No. Wo477/18, the VW Foundation and INTAS is gratefully acknowledged.

REFERENCES

1 T. Gutbrod, M. Bayer, A. Forchel, P.A. Knipp, T.L. Reinecke, A. Tartakovskii, V.D. Kulakovskii, N.A. Gippius, S.G. Tikhodeev: Phys. Rev. B **59**, 2223 (1999)
2 M.V. Artemyev, U. Woggon: Appl. Phys. Lett. **76**, 1355 (2000)
3 Y. Yamamoto, F. Tassone, H. Cao: *Semiconductor Cavity Quantum Electrodynamics*, Springer Tracts in Modern Physics, Vol. 169 (Springer-Verlag, Berlin 2000)
4 H. Benisty, J.M. Gerard, R. Houdre, J. Rarity, C. Weisbuch (Eds.): *Confined Photon Systems*, Lecture Notes in Physics, Vol. 531 (Springer Verlag, Berlin 1999)
5 G.S. Agarwal: J. Modern Optics **45**, (1998)
6 E. Burstein, C. Weisbuch (Eds): *Confined Electrons and Photons* (Plenum Press, New York 1995)
7 J.M. Gerard, B. Gayral: Physica E **9**, 131 (2001)
8 M. Bayer, A. Forchel, T.L. Reinecke, P.A. Knipp, S. Rudin: Phys. Stat. Sol. A **191**, 3 (2002)
9 V.S. Ilchenko, A.A. Savchenkov, A.B. Matsko, L. Maleki: J. Opt. Soc. Am. B **20**, 333 (2003)
10 S. Arnold, M. Khoshsima, I. Teraoka, S. Holler, F. Vollmer: Opt. Lett. **28**, 272 (2003)
11 S. Spillane, T. Kippenberg, K. Vahala: Nature **415**, 621 (2002)
12 M.D. Barnes, S.M. Mahurin, A. Mehta, B.G. Sumpter, D.W. Noid: Phys. Rev. Lett. **88**, 015 508 (2002)
13 W.V. Klitzing, R. Long, V.S. Ilchenko, J. Hare, V. Lefévre-Seguin: Opt. Lett. **26**, 166 (2001)
14 J.R. Buck, H.J. Kimble: Phys. Rev. A **67**, 033 806 (2003)
15 E.M. Purcell: Phys. Rev. **69**, 681 (1946)
16 I.I. Rabi: Phys. Rev. **51**, 652 (1937)
17 L. Allen, J.H. Eberly: *Optical Resonances and Two-Level Atoms* (Wiley, New York 1975)
18 G. Mie: Ann. Phys. (Leipzig) **25**, 377 (1908)
19 P. Debye: Ann. Phys. (Leipzig) **30**, 57 (1909)
20 J.A. Stratton: *Electrodynamic Theory* (MacGraw Hill, New York 1941)
21 M. Kerker: *The Scattering of Light and other Electromagnetic Radiation* (Academic Press, New York 1969)
22 H.C. van de Hulst: *Light Scattering by Small Particles* (Dover, New York 1981)
23 C.F. Bohren, D.R. Huffman: *Absorption and Scattering of Light by Small Particles* (Wiley, New York 1983)
24 P.W. Barber, S.C. Hill: *Light Scattering by Particles: Computational Methods* (World Scientific, Singapore 1990)
25 R.K. Chang, A.J. Campillo (Eds.): *Optical Processes in Microcavities*, Advanced Series in Appl. Physics, Vol. 3 (World Scientific, Singapore 1996)
26 S.C. Hill, R.E. Benner: J. Opt. Soc. Am. B **3**, 1509 (1986)
27 H. Chew: Phys. Rev. A **38**, 3410 (1988)
28 V.B. Braginsky, M.L. Gorodetsky, V.S. Ilchenko: Phys. Lett. A **137**, 393 (1989)
29 G. Chen, R.K. Chang, S.C. Hill, P.W. Barber: Opt. Lett. **16**,1269 (1991)
30 A.J. Campillo, J.D. Eversole, H.B. Lin: Phys. Rev. Lett. **67**, 437 (1991)
31 V. Sandoghdar, F. Treussart, J. Hare, V. Lefévre-Seguin, J.M. Raimond, S. Haroche: Phys. Rev. B **54**, R1777 (1996)
32 D.W. Vernooy, A. Furusawa, N.P. Georgiades, V.S. Ilchenko, H.J. Kimble: Phys. Rev. A **57**, R2293 (1998)
33 H.B. Lin, J.D. Eversole, A.J. Campillo, J.P. Barten: Opt. Lett. **23**, 1921 (1998)
34 V.V. Klimov, P.N. Lebedev, M. Ducloy, V.S. Letokhov: Phys. Rev. A **59**, 2996 (1999)
35 H. Fujiwara, K. Sasaki: J. Appl. Phys. **86**, 2385 (1999)
36 M.D. Barnes, C.Y. Kung, W.B. Whitten, J.M. Ramsey, S. Arnold, S. Holler: Phys. Rev. Lett. **21**, 3931 (1996)
37 S. Arnold, S. Holler, N.L. Goddard, G. Griffel: Opt. Lett. **22**, 1452 (1997)
38 S.C. Hill, H.I. Saleheen, M.D. Barnes, W.B. Whitten, J.M. Ramsey: Appl. Opt. **35**, 6278 (1996)
39 S.C. Hill, P. Nachman, S. Arnold, J.M. Ramsay, M.D. Barnes: J. Opt. Soc. Am. **16**, 1868 (1999)
40 C. Hafner: *The Generalized Multipole Technique for Computational Electromagnetism* (Artech House Books 1990)
41 H. Schniepp, V. Sandoghdar: Phys. Rev. Lett. **89**, 257 403 (2002)
42 M. Artemyev, U. Woggon, R. Wannemacher: Appl. Phys. Lett. **78**, 1032 (2001)
43 B. Möller, M.V. Artemyev, U. Woggon, R. Wannemacher: Appl. Phys. Lett. **80**, 3253 (2002)
44 R. Wannemacher, A. Pack, M. Quinten: Appl. Phys. B **67**, 1 (1998)
45 D.V. Talapin, A.L. Rogach, A. Kornowski, M. Haase, H. Weller: Nano Lett. **1**, 207 (2001)
46 C.B. Murray, D.J. Norris, M.G. Bawendi: J. Am. Chem. Soc. **115**, 8707 (1993)
47 L. Qu, X. Peng: J. Am. Chem. Soc. **124**, 2049 (2002)
48 M.A. Hines, P. Guyot-Sionnest: J. Phys. Chem. **100**, 468 (1996)
49 B.O. Daboussi, J. Rodriquez-Viejo, F.V. Mikulec, J.R. Heine, H. Mattoussi, R. Ober, K.F. Jensen, M.G. Bawendi: J. Phys. Chem. B **101**, 9463 (1997)
50 C. de Mello Donega, S.G. Hickey, S.F. Wuister, D. Vanmaekelbergh, A. Meijerink: J. Phys. Chem. B **107**, 489 (2003)
51 U. Woggon: *Optical Properties of Semiconductor Quantum Dots*, Springer Tracts in Modern Physics, Vol. 136 (Springer, Berlin 1996)
52 X. Peng, L. Manna, W. Yang, J. Wickham, E. Scher, A. Kadavanich, A.P. Alivisatos: Nature **404**, 59 (2000)
53 L. Manna, E.C. Scher, A.P. Alivisatos: J. Am. Chem. Soc. **122**, 12 700 (2000)
54 J. Hu, L. Li, W. Yang, L. Manna, L. Wang, A.P. Alivisatos: Science **292**, 2060 (2001)
55 Z.A. Peng, X. Peng: J. Am. Chem. Soc. **123**, 1389 (2001)
56 M. Nirmal, D.J. Norris, M. Kuno, M.G. Bawendi, A.L. Efros, M. Rosen: Phys. Rev. Lett. **75**, 3728 (1995)
57 A.L. Efros, M. Rosen, M. Kuno, M. Nirmal, D.J. Norris, M.G. Bawendi: Phys. Rev. B **54**, 4843 (1996)
58 M. Chamarro, C. Gourdon, P. Lavallard, O. Lublinskaya, A.I. Ekimov: Phys. Rev. B **53**, 1336 (1996)
59 U. Woggon, F. Gindele, O. Wind, C. Klingshirn: Phys. Rev. B **54**, 1506 (1996)
60 V.D. Kulakovskii, G. Bacher, R. Weigand, T. Kümmell, A. Forchel, E. Borovitskaya, K. Leonardi, D. Hommel: Phys. Rev. Lett. **82**, 1780 (1999)
61 X. Fan, M.C. Lonergan, Y. Zhang, H. Wang: Phys. Rev. B **64**, 115 310 (2001)
62 B. Patton, W. Langbein, U. Woggon: Phys. Rev. B (2003)
63 T. Förster, *Floureszenz Organischer Verbindungen* (Vandenhoeck and Ruprecht, Göttingen 1951)
64 G. Schlegel, J. Bohnenberger, I. Potapova, A. Mews: Phys. Rev. Lett. **88**, 137 401 (2002)
65 B. Lounis, H.A. Bechtel, D. Gerion, P. Alivisatos, W.E. Moerner: Chem. Phys. Lett. **329**, 399 (2000)
66 C.A. Leatherdale, W.K. Woo, F.V. Mikulec, M.G. Bawendi: J. Phys. Chem. B **106**, 7619 (2002)
67 U. Woggon, O. Wind, F. Gindele, E. Tsitsishvili, M. Müller: J. Luminescence. **70**, 269 (1996)
68 S.A. Empedocles, D.J. Norris, M.G. Bawendi: Phys. Rev. Lett. **77**, 3873 (1996)
69 U. Banin, M. Bruchez, A.P. Alivisatos, T. Ha, S. Weiss, D.S. Chemla: J. Chem. Phys. **110**, 195 (1999)
70 R.G. Neuhauser, K.T. Shimizu, W.K. Woo, S.A. Empedocles, M.G. Bawendi: Phys. Rev. Lett. **85**, 3301 (2000)
71 M. Kuno, D.P. Fromm, H.F. Hamann, A. Gallagher, D.J. Nesbitt: J. Phys. Chem. **115**, 1028 (2001)
72 P. Michler, A. Imamoglu, M.D. Mason, P.J. Carson, G.F. Strouse, S.K. Buratto: Nature **406**, 968 (2000)
73 M.V. Artemyev, U. Woggon, R. Wannemacher, H. Jaschinski, W. Langbein: Nano Lett. **1**, 309 (2001)
74 P. Palinginis, H. Wang: Appl. Phys. Lett. **78**, 1541 (2001)
75 P. Palinginis, S. Tavenner, M. Lonergan, H. Wang: Phys. Rev. B **67**, 201 307 (2003)

76 K. Takemoto, B.R. Hyun, Y. Masumoto: Solid State Comm. **114**, 521 (2000)
77 Y. Masumoto, M. Ikezawa, B.R. Hyun, K. Takemoto, M. Furuya: Phys. Stat. Sol. B **224**, 613 (2001)
78 C.E. Finlayson, D.S. Ginger, N.C. Greenham: Appl. Phys. Lett. **77**, 2500 (2000)
79 H.J. Eisler, V.C. Sundar, M.G. Bawendi, M. Walsh, H.I. Smith, V. Klimov: Appl. Phys. Lett. **80**, 4614 (2002)
80 X. Fan, S. Lacey, P. Palinginis, H. Wang, M. Lonergan: Opt. Lett. **25**, 1600 (2000)
81 J.M. Gerard, B. Sermage, B. Gayral, B. Legrand, E. Costard, V. Thierry-Meig: Phys. Rev. Lett. **81**, 1110 (1998)
82 G.S. Solomon, M. Pelton, Y. Yamamoto: Phys. Rev. Lett. **86**, 3903 (2001)
83 M. Bayer, T.L. Reinecke, F. Weidner, A. Larionov, A. McDonald, A. Forchel: Phys. Rev. Lett. **86**, 3168 (2001)
84 L.S. Li, A.P. Alivisatos: Phys. Rev. Lett. **90**, 097 402 (2003)
85 B. Möller, U. Woggon, M.V. Artemyev, R. Wannemacher: Appl. Phys. Lett., in press
86 M. Kazes, D.Y. Lewis, Y. Ebenstein, T. Mokari, U. Banin: Adv. Mat. **14**, 317 (2002)
87 G. Börk, A. Karlsson, Y. Yamamoto: Phys. Rev. A **50**, 1675 (1994)
88 P.V. Kelkar, V.G. Kozlov, A.V. Nurmikko: Phys. Rev. B **56**, 7564 (1997)
89 G. Björk, Y. Yamamoto: IEEE J. Quantum Electron. **QE-27**, 2386 (1991)
90 M. Pelton, Y. Yamamoto: Phys. Rev. A **59**, 2418 (1999)
91 A. Thränhardt, C. Ell, G. Khitrova, H.M. Gibbs: Phys. Rev. B **65**, 035 327 (2002)